PAPER

Check for updates

First-principles studies of enhanced oxygen reduction reactions on graphene- and nitrogen-doped graphene-coated platinum surfaces†

Ho Ngoc Nam, [ID] *[ab] Quan Manh Phung, [ID] [cd] Pongpol Choeichom,[a] Yusuke Yamauchi[bef] and Nagahiro Saito [ID] *[ag]

Developing innovative platinum-based electrocatalysts and enhancing their efficiency are crucial for advancing high-performance fuel cell technology. In this study, we employed DFT calculations to provide a theoretical basis for interpreting the impact of graphene coatings on various Pt surfaces on oxygen reduction reaction (ORR) catalytic activity, which are currently applied as protective layers in experiments. We comprehensively assess the geometric and electronic properties of Pt(100), Pt(110), and Pt(111) surfaces in comparison to their graphene-coated counterparts, revealing different adsorption behaviors of O_2 across these surfaces. The ORR mechanisms on different Pt surfaces show distinct rate-determining steps, with Pt(111) showing the highest ORR activity, followed by Pt(110) and Pt(100). Graphene coatings play a key role in enhancing charge transfer from the surface, resulting in modifications of O_2 adsorption. Despite influencing ORR kinetics, these graphene-coated surfaces demonstrate competitive catalytic activity compared to their bare counterparts. Notably, Pt(111) with a graphene coating exhibits the lowest activation energy among graphene-coated surfaces. Our calculations also suggest that the ORR can occur directly on non-defective Pt@graphene surfaces rather than being restricted to exposed Pt centers due to point defects on graphene. Furthermore, our work highlights the potential of nitrogen doping onto the Pt(111)@C surface to further enhance ORR activity. This finding positions nitrogen-doped Pt@C as a promising electrocatalyst for advancing electrochemical technologies.

1. Introduction

Global warming and the massive decline in fossil fuels in recent years have further proven the importance for humanity to transition towards the use of green, clean, and sustainable energy resources.[1] Advanced energy conversion technologies (*e.g.*, solar photovoltaics, thermoelectrics, geothermal power, *etc.*)[2–9] have made a significant contribution to the common effort to produce environmentally sustainable alternative energy sources. Notably, fuel cells have emerged as a promising technology for generating electricity through reactions involving oxygen and hydrogen.[10–12] Despite these advancements, a key challenge persists in the development of efficient and durable cathode catalysts for fuel cells. Specifically, the slow kinetics of the oxygen reduction reaction (ORR) occurring in the cathode are a primary bottleneck, resulting in a large proportion of potential loss.[13] Therefore, research on high-performance catalysts that can accelerate the ORR is highly required.

Despite its high cost and scarcity, platinum (Pt) remains popular as one of the most dynamic ORR electrocatalysts in commercialized proton exchange membrane fuel cells (PEMFCs).[13,14] Nevertheless, this type of material has certain drawbacks that limit its performance. According to Sabatier's principle,[15] the

a Institute of Materials Innovation, Institutes of Innovation for Future Society, Nagoya University, Furo-cho, Chikusa-ku, Nagoya 464-8601, Japan. E-mail: honam@sp.material.nagoya-u.ac.jp, hiro@sp.material.nagoya-u.ac.jp

b Department of Materials Process Engineering, Graduate School of Engineering, Nagoya University, Nagoya 464-8603, Japan

c Department of Chemistry, Graduate School of Science, Nagoya University, Furo-cho, Chikusa-ku, Nagoya 464-8602, Japan

d Institute of Transformative Bio-Molecules (WPI-ITbM), Nagoya University, Furo-cho, Chikusa-ku, Nagoya 464-8601, Japan

e Australian Institute for Bioengineering and Nanotechnology (AIBN), The University of Queensland, Brisbane, QLD 4072, Australia

f Department of Chemical and Biomolecular Engineering, Yonsei University, Seoul 03722, South Korea

g Department of Chemical Systems Engineering, Graduate School of Engineering, Nagoya University, Nagoya 464-8603, Japan

† Electronic supplementary information (ESI) available. See DOI: https://doi.org/10.1039/d4cp00269e

This journal is © the Owner Societies 2024

Phys. Chem. Chem. Phys., 2024, **26**, 10711–10722 | **10711**

interaction between the catalyst and the reactant should neither be too weak nor too strong. The pronouncedly strong bond between Pt and oxygen could thereby inhibit the efficient progress of the ORR activity and slow down the overall reaction. For example, it has been reported that alloying transition metals (*e.g.*, Fe, Co, Ni, or Cu) with Pt has the potential not only to reduce material costs but also to help improve the ORR performance of the catalyst.[16–18] This might be due to the electronic structure of Pt-based alloys being different from that of pure Pt, resulting in significant changes in how reactants and catalysts bond together and thereby improving ORR activity. Alternatively, materials derived from metal–organic frameworks (MOFs), offering large specific surface areas and different pore sizes,[19–21] as well as single-atom catalysts with tunable electronic structures,[22–28] are promising for further exploration of ORR electrocatalysis.

Moreover, catalytic durability is the next challenge for PEMFCs. Operating in harsh environments like high temperatures, strong acidic media, or high-potential regions could lead to a significant degradation of Pt catalysts over time.[29] Other adverse factors, such as particle coalescence, dissolution, and poisoning, could even make this degradation worse.[30,31] As a result, the catalytic activity and overall performance of fuel cells significantly decrease. In previous studies,[32,33] MgO and SnO$_2$ used as coatings have shown effectiveness in improving the durability and stability of Pt-based catalysts. Unfortunately, these coatings also hindered ORR activity on the catalyst surface due to the poor conductivity and blocking of the active sites.[34] Therefore, enhancing both the catalytic performance and durability of Pt catalysts is crucial.

Graphene is a well-known material for its outstanding electrical conductivity, high surface area, and chemical stability.[35] It can form specific solid-state ligand bonds to augment electron transfer with metals.[36] Recently, several studies have applied graphene as an effective coating for Pt-based catalysts.[37–40] For instance, it was found that Pt-based nanoparticles with graphene encapsulation fabricated *via* the solution plasma process improved not only the durability but also the efficient ORR activity of the catalysts.[34,41] This suggests the great potential of graphene coatings for catalytic applications. Moreover, it was found that nitrogen-doped graphene could be beneficial in enhancing the ORR catalytic performance compared to pure graphene.[42] However, the properties of these graphene coatings on Pt surfaces and how they influence the ORR activity of the system have not been clear yet. Previous theoretical studies mainly investigated the ORR mechanism on bare Pt surfaces with various models (*e.g.*, clusters[43–45] and slabs[46–48]) using different exchange–correlation functionals (*i.e.*, PBE,[43] PBE-D3,[45] SCAN-rVV10,[49] PW91,[48] B3LYP,[50] and PZ[51]), making comparisons and analysis of the related properties difficult. Furthermore, some studies on the ORR mechanism on graphene-supported Pt nanoparticles[52,53] or single Pt atom-supported graphene[54,55] have also been done. However, not many studies related to the graphene coating on Pt surfaces have been reported.[49] It should be noted that bare Pt surfaces with different energies might have different effects on the

geometric and electronic structures of the graphene coatings, leading to significant changes in the ORR activity of catalysts. Therefore, elucidating the role of graphene coatings in the ORR performance is necessary.

In this work, we systematically investigated the mechanism of the oxygen reduction reaction on graphene-coated Pt surfaces. First, a slab model of low-index Pt facets is constructed, and ORR activity on these bare surfaces is investigated. After that, we discuss the changes in the geometric and electronic structure of systems when graphene is coated. The effect of the graphene coating on ORR activity is then revealed *via* the calculation of charge density and overpotential. Finally, the influence of nitrogen doping on the graphene coating is also discussed, suggesting its potential to reduce the system's overpotential as compared to the pristine graphene layer.

2. Computational methods and models

Our DFT calculations are performed using the projector-augmented wave[56] (PAW) potential as implemented in the Quantum-ESPRESSO package.[57] For the PAW potentials, the PSLIBRARY version 1.0.0 was adopted.[58] The wave functions and augmentation charge density in terms of a plane-wave basis set were expanded with kinetic energy cut-offs of 50 and 400 Ry, respectively. The spin polarization was taken into account in the calculations. A Gaussian smearing of 0.02 Ry was also added to treat the Fermi surface. For the exchange–correlation, a generalized gradient approximation (GGA) functional in the form of Perdew–Ernzerhof–Burke[59] (PBE) functional was employed along with Grimme's van der Waals (vdW) correction[60] (D3) to describe the weak dispersion interactions between the adsorbates and the surfaces. It should be noted that the use of different functionals possibly enhances the accuracy of the results but is computationally demanding, which is therefore not considered in this current work. Instead, only the PBE-D3 functional was used throughout the calculations to systematically and comprehensively evaluate how the graphene coating affects ORR activity.

To analyze the stability of pristine Pt facets, we estimated their surface formation energy as follows:

$$\gamma = \frac{1}{2A}\left(E_{\text{slab}}^{\text{total}} - nE_{\text{bulk}}^{\text{atom}}\right) \quad (1)$$

where A, $E_{\text{slab}}^{\text{total}}$, $E_{\text{bulk}}^{\text{atom}}$, and n are the surface area, the total energy of the surface slab, the bulk energy per atom, and the number of atoms in the slab, respectively. Besides, since the binding energy of adsorbates on surfaces is relative to the electronic structure of the surface itself, we estimated the d- and p-band center model,[61,62] which was proposed by Hammer and Nørskov to discuss their role in surface interactions:

$$\varepsilon_{\text{d,p}} = \frac{\int_{-\infty}^{+\infty} n_{\text{d,p}}(\varepsilon)\varepsilon\,\text{d}\varepsilon}{\int_{-\infty}^{+\infty} n_{\text{d,p}}(\varepsilon)\,\text{d}\varepsilon} \quad (2)$$

where $n_{\text{d,p}}(\varepsilon)$ and ε are the density and energy of d- or p-states, respectively. A graphene-coated platinum (Pt@C) model was

10712 | *Phys. Chem. Chem. Phys.*, 2024, **26**, 10711–10722

This journal is © the Owner Societies 2024

then constructed from a Pt slab with five layers of atoms in the z-direction and a graphene layer covering the top side of the slab. A vacuum region of 20 Å was inserted between neighboring surfaces to eliminate undesired coulombic interactions between the model and its self-images caused by periodic boundary conditions. Except for the two bottom layers that were fixed, the remaining atoms in the system were allowed to relax until the residual forces were less than 0.002 Ry bohr^{-1} with a $4 \times 4 \times 1$ k-point grid. Here, we consider three slab models representing the three low-index facets, including Pt(100)@C, Pt(110)@C, and Pt(111)@C. Specifically, the Pt(100)@C system generated by interfacing a 2×5 unit cell of Pt(100) with a $2 \times 3\sqrt{3}$ unit cell of graphene; the Pt(110)@C system constructed by interfacing a 2×5 unit cell of Pt(110) with a $2 \times 4\sqrt{3}$ unit cell of graphene; and the Pt(111)@C system created by interfacing a 3×3 unit cell of Pt(111) with a 3×3 unit cell of graphene. The choice of different cell sizes for surfaces is to ensure the lattice mismatch between the Pt surfaces and graphene layers is minimal. These models correspond to a low adsorption coverage of O_2. We note that the graphene sheet can have many different orientations on the metal surfaces. In this study, we only adopted orientations that lead to a moderate interaction between graphene and Pt surfaces, which is believed to increase the adsorption energy between graphene and O_2.
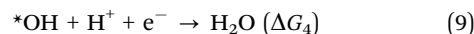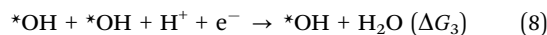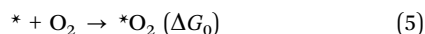
The adsorption energy of an intermediate is defined by:

$$E_{ads} = E_{system} - (E_{catalyst} + E_{adsorbate}) \quad (3)$$

where E_{system}, $E_{catalyst}$, and $E_{adsorbate}$ are the total energy of combined systems, isolated surface systems, and isolated adsorbates, respectively. To consider the catalytic activity for ORR processes, the Gibbs free energy of individual adsorbates at pressure $P = 1$ atm is investigated by adding up their adsorption energy along with corrections from zero-point energy (E_{ZPE}) and entropy (S) at $T = 298.15$ K as follows

$$G(T, P) = E_{elec} + E_{ZPE} + \int_0^T C_p dT - TS(T, P) \quad (4)$$

where E_{elec} is the electronic energy, $E_{ZPE} = \sum_i^N \frac{h\nu_i}{2}$ is the zero-point energy with ν_i being the vibrational frequency of N modes obtained from the finite displacement method in an atomic simulation environment (ASE),[63] and C_p is the heat capacity involving translational, rotational, vibrational, electronic parts, and a k_B term. It should be noted that for ideal gas cases (*e.g.*, H_2 and H_2O), translational and rotational degrees of freedom were taken into account. For adsorbates, however, all degrees of freedom of the adsorbate are treated harmonically since they often have no real translational or rotational degrees of freedom. The associative ORR mechanisms are then investigated *via* the four-electron pathway in an acidic medium (*i.e.*, pH = 0) with intermediates including:[64]

$$* + O_2 \rightarrow {}^*O_2 \ (\Delta G_0) \quad (5)$$

$$^*O_2 + H^+ + e^- \rightarrow {}^*OOH \ (\Delta G_1) \quad (6)$$

$$^*OOH + H^+ + e^- \rightarrow {}^*OH + {}^*OH \ (\Delta G_2) \quad (7)$$

$$^*OH + {}^*OH + H^+ + e^- \rightarrow {}^*OH + H_2O \ (\Delta G_3) \quad (8)$$

$$^*OH + H^+ + e^- \rightarrow H_2O \ (\Delta G_4) \quad (9)$$

where * represents the active site of catalysts. We note that on some surfaces, the hydrogenation of $^*O_2$ can directly lead to $^*O$ and $^*OH$ *via* transient $^*OOH$.[65] It is well-known that the high-spin ground state of the O_2 molecule is poorly described in DFT calculations,[66] so we therefore derived its free energy *via* the relation to $H_2O(l)$ and $H_2(g)$ as G_{O_2} (eV) $= 2G_{H_2O} - 2G_{H_2} + 4 \times 1.23$. The change in Gibbs free energy (in eV) of intermediates ΔG_i can be calculated using

$$\Delta G_0 = G_{*O_2} - G_* - 2G_{H_2O} + 2G_{H_2} - 4.92 \quad (10)$$

$$\Delta G_1 = G_{*OOH} - G_{*O_2} - \frac{1}{2}G_{H_2} \quad (11)$$

$$\Delta G_2 = G_{*OH + *OH} - G_{*OOH} - \frac{1}{2}G_{H_2} \quad (12)$$

$$\Delta G_3 = G_{*OH} + G_{H_2O} - G_{*OH + *OH} - \frac{1}{2}G_{H_2} \quad (13)$$

$$\Delta G_4 = G_{H_2O} + G_* - G_{*OH} - \frac{1}{2}G_{H_2} \quad (14)$$

Finally, the overpotential (η_{ORR}, in V) could be estimated using Nørskov's model with a lower overpotential implying better ORR performance.[66]

$$\eta_{ORR} = 1.23 - U_L \quad (15)$$

where U_L is the limiting potential, which corresponds to the minimum free energy change among reaction steps

$$U_L = -\min(\Delta G_1, \Delta G_2, \Delta G_3, \Delta G_4) \quad (16)$$

Finally, it is important to note that solvent effects were not considered. However, previous research by Iyemperumal and Deskins[67] found that on the Pt(111) surface, solvent effects (especially for small species investigated for the ORR such as O_2, O, and OH) are minimal. For example, the solvation energy of O_2 on Pt(111) is only 0.01 eV. Additionally, in a recent related work on the ORR performance of a single-layer Pt–graphene hybrid,[49] it was found that the use of the implicit solvation model could affect the ORR performance of hybrid Pt–graphene, however, the energy difference is not significant.

3. Results and discussion

3.1. Geometric and electronic structures of bare Pt and Pt@C surfaces

First, we examine the structures and the corresponding surface energies of bare Pt facets, as illustrated in Fig. 1. Notably, Pt(111) emerges as the most stable facet, having a surface energy of 0.120 eV Å^{-2} owing to its larger planar density. In contrast, Pt(110) and Pt(100) exhibit significantly higher surface energies (0.174 and 0.162 eV Å^{-2}, respectively),
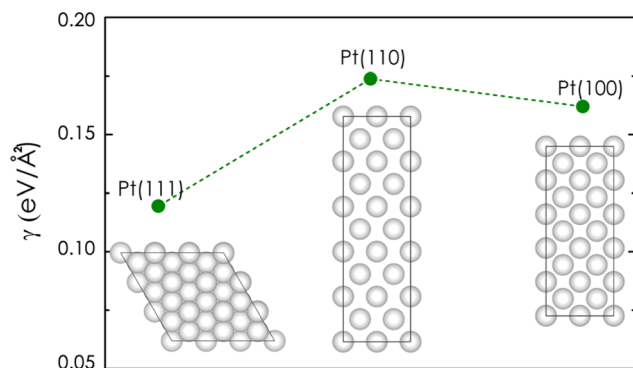
Fig. 1 The calculated surface energy corresponds to three different low-index Pt facets, including Pt(100), Pt(110), and Pt(111).

reflecting their lower planar density and higher number of dangling bonds. The less stable Pt(110) and Pt(100) surfaces are thereby ready to form additional bonds with adsorbates to stabilize their structures. As a result, the geometry of graphene coatings on Pt(100) and Pt(110) could be different from that on Pt(111). Because of the interaction of Pt(100) and Pt(110) surfaces with the graphene top layer [see Fig. 2(a and b)], their bonds exhibit considerable strength with an average distance of approximately 2.1–2.2 Å, indicative of some covalent character as shown by the electron localization function calculations (Fig. S1, ESI†). Remarkably, the graphene layer undergoes distortion from its planarity. This reduces the stress due to lattice misfit between graphene and the metal surfaces. The maximum buckling in the carbon layer reaches around 0.33 Å on Pt(100) and Pt(110), while the C–C bond distance ranges from 1.467 to 1.570 Å. In contrast, Pt(111) exhibits higher surface stability, resulting in the physisorption of graphene [Fig. 2(c)]. The Pt(111)–graphene distance is 2.7 Å, which is in

fair agreement with the distance estimated in previous work by Wang *et al.*[68] (*i.e.*, 3.3 Å). The small mismatch between the Pt(111) unit cell and graphene (1.08%) minimizes the distortion, allowing graphene to maintain planarity, albeit with an increased C–C bond distance from 1.424 Å (in isolated graphene) to 1.556 Å. In fact, the adsorption of graphene on Pt(111), in several Moiré patterns G/Pt(111)-$(\sqrt{3} \times \sqrt{3})R30°$ (this work), G/Pt(111)-$(\sqrt{7} \times \sqrt{7})R19.1°$, and G/Pt(111)-$(2\sqrt{13} \times 2\sqrt{13})R13.9°$, has been experimentally shown to be very weak.[69,70]

Moreover, we also look at the electronic structure of these surfaces. The density of states (DOS) along with the partial density of states (pDOS) is depicted in Fig. 3. According to the d-band center theory proposed by Nørskov *et al.*,[61,62,71] the adsorption energy of the adsorbate is related to the relative energy between the d-states and the Fermi level. Simply put, the higher the d-states, the more empty the anti-bonding states, and the stronger the adsorption. The calculated energy of the d-band center (ε_d) stands at −2.637, −2.570, and −2.729 eV for Pt(100), Pt(110), and Pt(111), respectively. The estimated ε_d of Pt(111) closely aligns with values previously estimated by Hammer *et al.*[72] The highest d-band center of Pt(110) indicates that this surface should have the strongest adsorption, whereas the adsorption ability of Pt(111) should be the weakest (see Table 1 for the case of O_2). This tendency matches well the trend of the surface energy above, *i.e.*, the least stable surface has the highest adsorption energy.

As graphene is coated on Pt surfaces, the d-band center slightly shifts to values of −2.712, −2.675, and −2.781 eV for Pt(100)@C, Pt(110)@C, and Pt(111)@C, respectively [see Fig. 3(b)]. This indicates that, if O_2 could penetrate the graphene layer to interact with the Pt surface (see ref. 73), the anticipated interaction would be weaker than that observed on the pristine Pt surface. However, since adsorbates directly
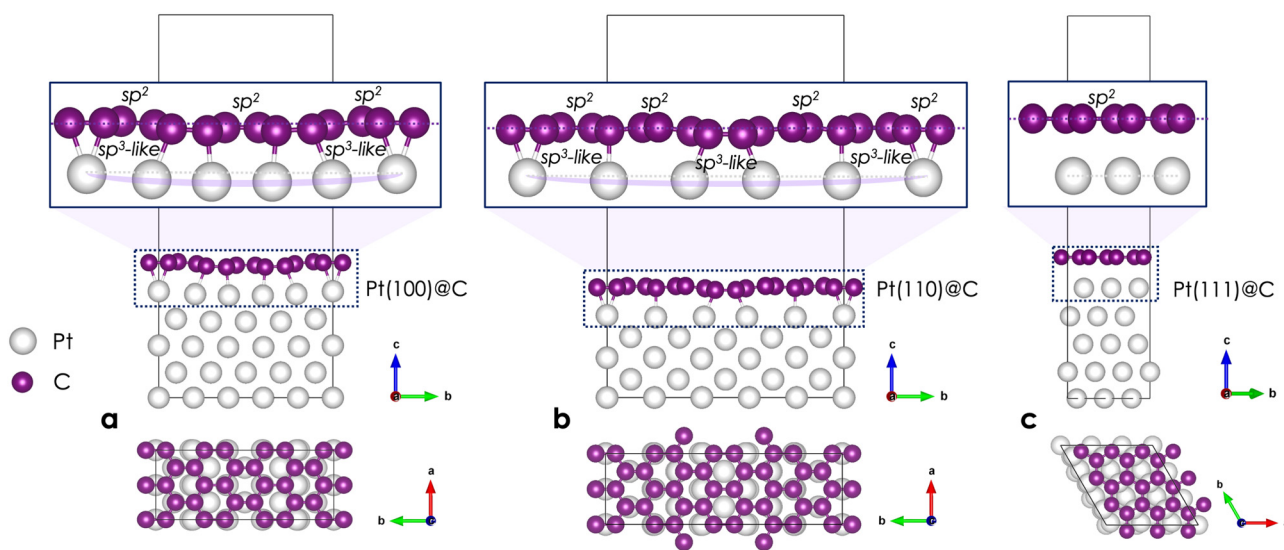

Fig. 2 The side and top views of graphene-coated platinum models used for calculations include (a) Pt(100)@C, (b) Pt(110)@C, and (c) Pt(111)@C. The purple and grey balls represent C and Pt atoms, respectively. The distortion of graphene surfaces due to Pt–C covalent bonds induces two different sp^2 and sp^3-like hybridizations of carbon.
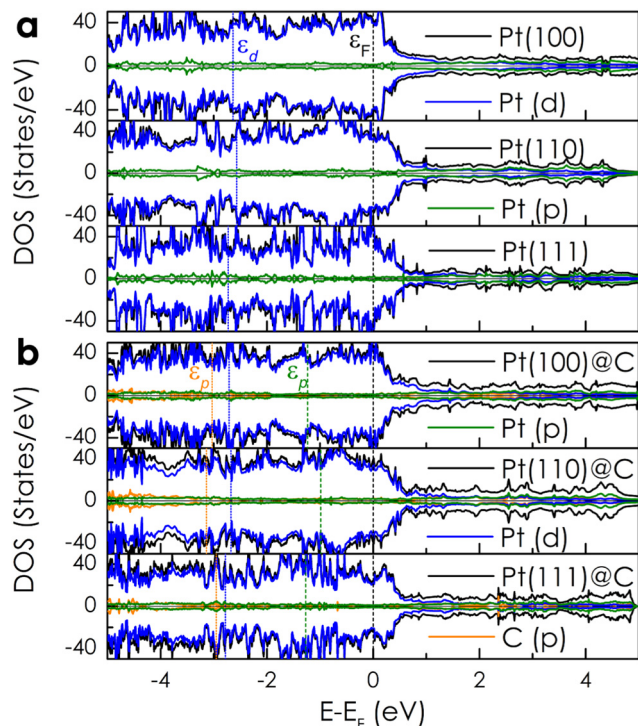
10714 | *Phys. Chem. Chem. Phys.*, 2024, **26**, 10711–10722

This journal is © the Owner Societies 2024

Fig. 3 Total DOSs and partial DOSs of (a) bare Pt and (b) Pt@C surfaces. The Fermi level (ε_F, black dashed line) is found at 0 eV. Positions of the C p-band center (ε_p, orange vertical line), Pt p-band center (ε_p, green vertical line), and Pt d-band center (ε_d, blue vertical line) are marked for comparison.

interact with the graphene surface in Pt@C, the specific location of d-band centers is less relevant. Indeed, the adsorption of O_2 on Pt(100)@C is the strongest (Table 1), whereas the d-band center of Pt in Pt(100)@C is not the highest. Similarly, the p-band centers of Pt in Pt@C (-1.234, -0.987, and -1.270 eV for Pt(100)@C, Pt(110)@C, and Pt(111)@C, respectively) also do not correlate well with the adsorption energy tendency. We instead look at the carbon p-band center as an alternative descriptor for the adsorption on non-metallic surfaces. The calculated p-band center of C is at -3.030, -3.138, and -2.954 eV for Pt(100)@C, Pt(110)@C, and Pt(111)@C, respectively. It is then assumed that Pt(110)@C has weaker adsorption than the other surfaces. However, the results of adsorption energy (see Table 1) invalidate this assumption, *e.g.*, the

Pt(110)@C surface adsorbs stronger than Pt(111)@C. This observation can be easily understood as the adsorption of O_2 not only depends on the interaction between O_2 and graphene but also on the interaction between the (mobile) graphene layer and the top layer of Pt. Indeed, upon O_2 adsorption, the distance between graphene and the Pt surfaces significantly changes (*vide infra*). Therefore, solely looking at the p-band center will not give the correct trend of O_2 adsorption on these graphene-coated surfaces. Furthermore, due to the buckling of graphene layers on Pt(110) and Pt(100), the electronic structure of graphene is expected to change, in which the hybridization of some carbon atoms deviates from a perfect sp^2 towards sp^3. Such a change in hybridization has been linked to the ability of graphene to bind to O_2. The change of hybridization is also associated with the formation of additional Pt–C bonds (Fig. S1, ESI†). We therefore referred to these carbons as "sp^3-like", as their character should lie between sp^2 and sp^3.

To conclude, our data clearly show that, whereas the d-band center of Pt is a good indicator of the adsorption strength on the bare Pt surfaces, neither it nor the p-band center of graphene can be used to explain the adsorption trend of O_2 on the Pt@C surfaces.

3.2. O_2 adsorption on Pt and Pt@C surfaces

In Table 1, we present the adsorption energy of O_2 on both bare graphene, Pt surfaces, and graphene-coated Pt surfaces, along with the corresponding bond distances between O, Pt, and C atoms. The stable adsorption configurations are visually illustrated in Fig. 4.

On graphene, the adsorption is primarily physisorption, characterized by a modest adsorption energy of only -0.12 eV and a relatively long distance between O_2 and graphene (~ 3.4 Å). Our calculated adsorption energy is in excellent agreement with a recent experimental value of -0.15 eV[76] as well as a diffusion Monte Carlo result (-0.14 eV).[77] The O_2 molecule is found to be parallel to the surface and maintains its triplet spin state. The O–O equilibrium bond distance is 1.23 Å, being close to the bond length of 1.21 Å in its isolated state. The resulting charge transfer between O_2 and graphene remains minimal, amounting to less than 0.1 electrons [see also Fig. 5(c)]. It should be noted that while the O_2 singlet can be chemisorbed on graphene (with a C–O bond length of ~ 1.5 Å), it is highly unstable. The adsorption energy of a singlet-O_2 on graphene was estimated to be highly positive (~ 1.8 eV).[75]

Table 1 Adsorption energy (in eV) of O_2 on different surfaces; bond distances between O, Pt, and C atoms (in Å); and the amount of charge transferred from the surface to O_2 ΔQ

Surface	E_{ads} (eV)	$d_{X–O}$ (Å) [X = Pt, C]	$d_{O–O}$ (Å)	ΔQ
Pt(100)@C	-1.02	1.476	1.486	-0.95
Pt(110)@C	-0.59	1.480	1.490	-0.91
Pt(111)@C	-0.32	1.477	1.489	-0.97
Pt(100)	-1.22	1.983	1.370	-0.49
Pt(110)	-1.52	1.968	1.368	-0.53
Pt(111)	-0.70 (-0.72,[a] -0.84,[b] -1.11[b])	2.036	1.358	-0.48
Graphene	-0.12 (-0.13,[c] -0.15[d])	3.380	1.230	-0.09

[a] Ref. 51. [b] Ref. 49. [c] Ref. 74. [d] Ref. 75.

This journal is © the Owner Societies 2024

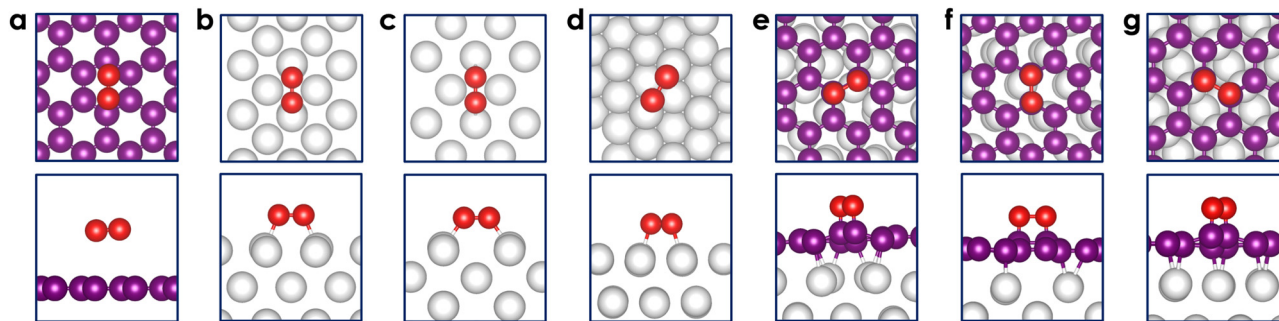*Phys. Chem. Chem. Phys.*, 2024, **26**, 10711–10722 | **10715**

Fig. 4 Stable configurations of O$_2$ adsorption on (a) graphene, (b) Pt(100), (c) Pt(110), (d) Pt(111), (e) Pt(100)@C, (f) Pt(110)@C, and (g) Pt(111)@C surfaces from top and side views. The red, purple, and grey balls represent O, C, and Pt atoms, respectively.
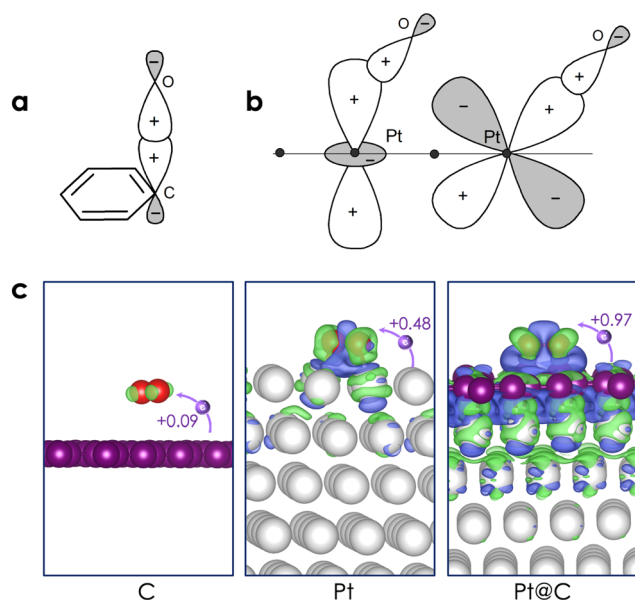
Fig. 5 (a) Interaction between C(sp^3)–O(sp^3), (b) Pt(d$_{z^2}$)–O(sp^3) and Pt(d$_{xz}$)–O(sp^3). (c) Charge transfers between O$_2$ and three surfaces: graphene, Pt(111), and Pt(111)@C. Color code: green: gaining electron region, blue: losing electron region (isosurface value of 0.002 e bohr^{-3}). The red, purple, and grey balls represent O, C, and Pt atoms, respectively.

On the bare Pt surfaces, O$_2$ is strongly chemisorbed, with an adsorption energy of −0.7 eV to −1.5 eV. In all cases, O$_2$ is parallel to the surfaces and is characterized as a closed-shell singlet species. As previously discussed, the Pt(111) surface, being the most stable among the three bare surfaces, displays the weakest adsorption. The calculated value of −0.7 eV is in good agreement with previously reported values ranging from −0.72 eV to −1.11 eV.[49,51] Notably, O$_2$ is found to bridge two adjacent Pt atoms, also referred to as the top–bridge–top (t–b–t) site.[78] At this site, the distance between O$_2$ and the surface measures approximately ∼2.0 Å, with the O–O bond distance elongated to ∼1.36 Å. A charge transfer from Pt(111) to the π⋆ orbital of O$_2$ is estimated at 0.5 electrons [see Fig. 5(b)]. This observation clearly indicates that the character of the adsorbed O$_2$ molecule is somewhere between that of an isolated O$_2$ and a superoxo O$_2^-$ species.

In comparison to the Pt(111) surface, the adsorption behavior of O$_2$ on Pt(110) and Pt(100) is quite similar. The distance between O$_2$ and the surfaces is slightly shorter, ranging from 1.97 to 1.98 Å, and the O–O bond exhibits a slight weakening with a bond distance of 1.37 Å. Remarkably, the binding of O$_2$ on Pt(110) is significantly stronger, manifesting as an adsorption energy of −1.5 eV. On this surface, O$_2$ could be adsorbed along the [1̄10] or [001] direction, referred to as top–short–bridge–top (t–sb–t) or top–long–bridge–top (t–lb–t) configurations, respectively. The latter configuration is found to be more stable than the former by 0.2 eV. It is important to note that a clean Pt(110) surface may undergo reconstruction, forming a missing-row type structure.[79–81] Such structural changes facilitate dissociative chemisorption of O$_2$,[82] though this aspect is not considered in this work. Also, a recent Raman spectroscopy experiment showed that the oxygen reduction reaction (ORR) on the three Pt facets under acidic conditions most likely proceeds through molecular oxygen instead of atomic oxygen.[83] On the unreconstructed Pt(100) surface, O$_2$ adsorbs at the bridge site (t–b–t configuration) with an adsorption energy of −1.22 eV, closely matching the results obtained in the work of Duan and Wang[48] employing the PW91 functional (−1.10 eV).

The adsorption of O$_2$ on graphene-coated surfaces is also summarized in Table 1 and Fig. 4(e–g). The important finding is that, in contrast to the bare graphene surface, O$_2$ chemisorbs on graphene-coated Pt surfaces with adsorption energies ranging from −0.3 eV to −1.0 eV. These negative values indicate the potential of Pt@C as a promising candidate for the ORR. Various configurations of O$_2$ on the three Pt@C were investigated, revealing a preference for the parallel orientation to the graphene layer in a top–top (t–t) configuration. The distance between carbon and oxygen is ∼1.48 Å, while the O–O bond length increases to around 1.49 Å. The C–O bond distance closely mirrors the values typically found in epoxides, whereas the O–O bond length resembles that of peroxide. As compared to the bare Pt surfaces, the strength of the O–O bond on Pt@C is clearly weaker. This difference can be attributed to the enhanced directional nature of the C(sp^3)–O(sp^3) bond, as illustrated in Fig. 5(a). On the other hand, the Pt–O bond manifests as either Pt(d$_{z^2}$)–O(sp^3) (displaying less directionality) or Pt(d$_{xz}$)–O(sp^3) (exhibiting more directionality).

Upon binding with O$_2$, two carbon atoms change their hybridization to sp^3, leading to a further distortion of the

10716 | *Phys. Chem. Chem. Phys.*, 2024, **26**, 10711–10722

This journal is © the Owner Societies 2024

graphene layer and inducing additional sp^3 carbons. The C–O covalent bonds not only alter the structure of the graphene layer but also influence the interaction between the graphene layer and Pt. For instance, while the interaction between Pt(111) and graphene is diffusive, the introduction of O_2 adsorption is responsible for the formation of more covalent bonds between C-sp^3 and Pt. In terms of the electronic structure, the adsorbed O_2 molecule can be characterized as a superoxide O_2^- species, as we found that 0.9–1.0 electrons were transferred from the surface to O_2 [Fig. 5(c)]. More interestingly, the charge transfer process involves not only the graphene layer but also the first and second layers of the Pt surface.

3.3. ORR mechanism on Pt and Pt@C surfaces

The associative ORR mechanisms on six surfaces including Pt(100), Pt(110), Pt(111), and their corresponding graphene-coated counterparts, Pt(100)@C, Pt(110)@C, Pt(111)@C are summarized in Fig. 6. Following the well-established computational protocol for the ORR, we only focus on four intermediates along the reaction: $*O_2$, $*O$–$*OH$, $*OH$–$*OH$, and $*OH$. Specifically, $*O_2$ is the starting active species of the ORR on all surfaces. We noted that OOH^+, as discussed in a recent work of Gueskine et al.,[84] is not a viable species in aqueous acidic media. They calculated that the proton exchange reaction $O_2 + H_3O^+ \rightarrow OOH^+ + H_2O$ is endothermic by 2.65 eV.
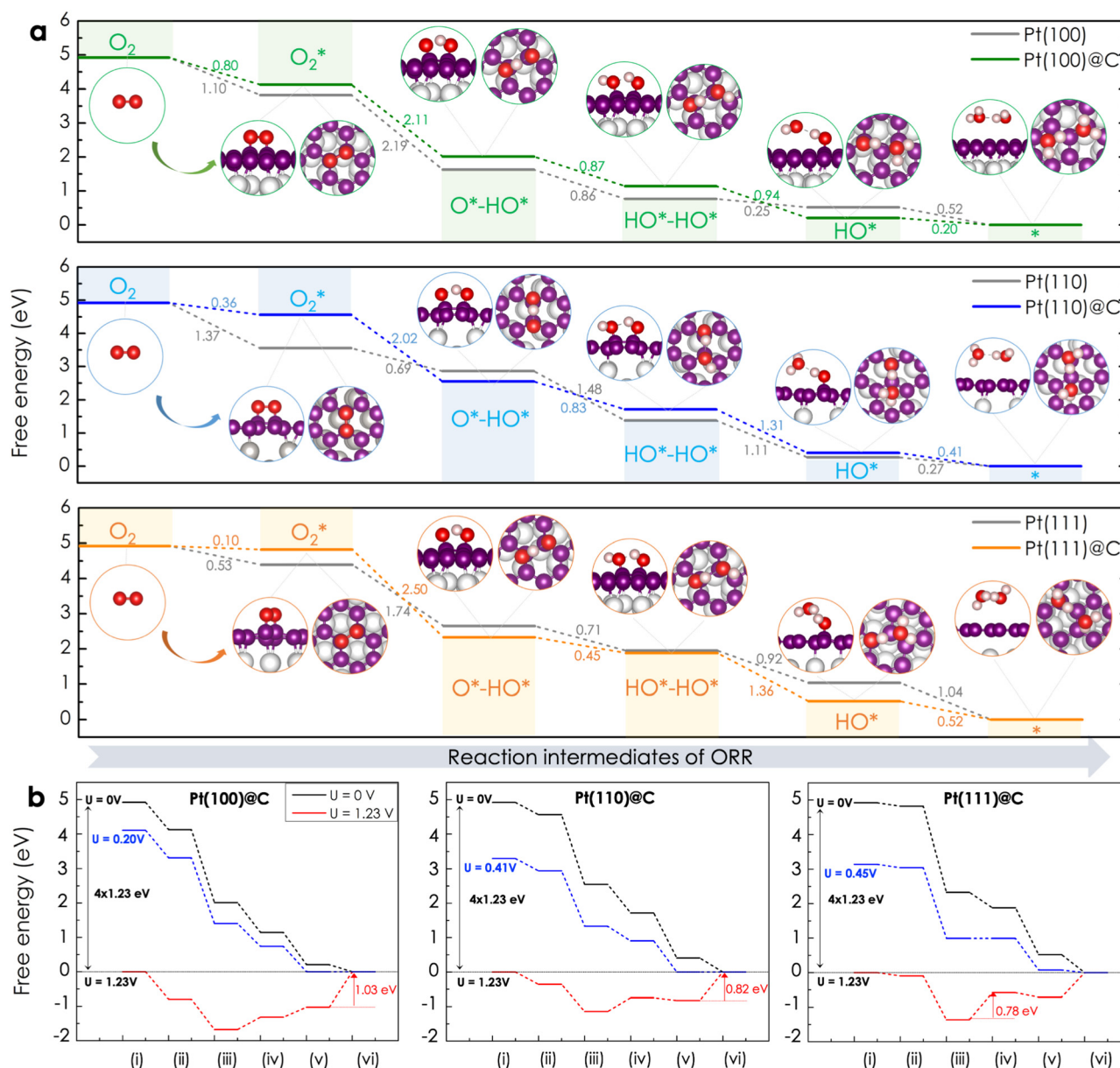

Fig. 6 (a) Free energy diagram and structures of ORR intermediates on Pt(100)@C (green steps line), Pt(110)@C (blue steps line), and Pt(111)@C (orange steps line) at $U_{RHE} = 0$ V, where U_{RHE} is the potential of the electrode relative to the RHE. The red, purple, grey, and white balls represent O, C, Pt, and H atoms. Free energy of the corresponding bare Pt surfaces (grey steps line) is inserted for comparison. (b) Free energy profile of the ORR on the graphene-coated surfaces at $U_{RHE} = 0$ V (in black), $U_{RHE} = 1.23$ V (in red), and limiting potential U_L (in blue).

Therefore, OOH$^+$ should not be the starting active species, as its concentration is negligible. They also pointed out that numerous researchers have fallen into this trap by picking up OOH$^+$ as the starting active species of ORR simulations.

Although OOH$^+$ is not the starting active species, the formation of *OOH on the surface is still plausible. This intermediate could be directly formed from the first hydrogenation of *O$_2$. Thus, we also calculated the *OOH species on all surfaces (see Fig. S2, ESI†). On all surfaces, the first hydrogenation of *O$_2$ can yield either *OOH or *O–*OH. Interestingly, *O–*OH is systematically more stable than *OOH by ∼2.0 eV on Pt(100) and Pt(100)@C; ∼1.0 eV on Pt(110) and Pt(110)@C; and ∼1.4 eV on Pt(111) and Pt(111)@C. On the Pt(111) surface, a similar value of 1.51 eV was also found by Duan and Wang.[85] On a carbon alloy catalyst, Chai et al.[86] also reported the instability of *OOH. Given the significant stability of *O–*OH, it is likely that once *OOH is formed, it is rapidly decomposed into *O–*OH. Indeed, on the Pt(111) surface, the activation energy for the *OOH dissociation reaction is negligible (0.05 eV).[85]

Let us first discuss the reactivity of the three bare Pt surfaces. Here, we focus only on the associative mechanism involving the *O–*OH intermediate. The mechanism with the *OOH species is discussed in the ESI.† In general, all surfaces possess similar ORR mechanisms, summarized as O$_2$ + 4(H$^+$ + e$^-$) → *O$_2$ + 4(H$^+$ + e$^-$) → *O + *OH + 3(H$^+$ + e$^-$) → *OH + *OH + 2(H$^+$ + e$^-$) → H$_2$O + *OH + (H$^+$ + e$^-$) → 2H$_2$O. Each surface exhibits different gaps between the reaction intermediates, resulting in different rate-determining steps (RDSs). At the electrode potential U_{RHE} (versus the reversible hydrogen electrode (RHE)) of zero, the free energy profiles are all downhill along the reaction pathway, i.e., all reduction steps are exergonic. For example, on Pt(111), the reduction free energies are −1.74, −0.71, −0.92, and −1.04 eV (Fig. S2, ESI†). The gaps between the intermediates can then be adjusted by changing the working potential. Specifically, the Gibbs free energy of the intermediates shifts by an amount of $-neU_{RHE}$, where n represents the number of electrons. On Pt(111), at the limiting potential U_L = 0.71 V, the reduction free energies change to −1.03, 0, −0.21, and −0.33 eV (Fig. S3, ESI†). Beyond this electrode potential, one of the reduction steps (the second reduction step *O–*OH + (H$^+$ + e$^-$) → *OH–*OH) becomes endergonic. When the electrode potential U_{RHE} is increased to 1.23 V, this reaction step has a reaction free energy of 0.52 eV, which corresponds to the RDS. This result is in line with the study of Duan and Wang,[48] in which the authors found the same RDS with an activation energy of 0.79 eV.

Hereafter, we will focus our discussion on the ORR at an electrode potential U_{RHE} of 1.23 V. For the Pt(110) surface, the RDS is the last reduction (*OH hydrogenation). The result agrees with the calculations reported by Dong et al.,[83] where they estimated an activation free energy of 1.18 eV. In our study, we estimated a slightly lower activation free energy of 0.96 eV. For the Pt(100) surface, the RDS is related to the third reduction step (*OH–*OH + (H$^+$ + e$^-$) → *OH + H$_2$O), which has an activation free energy of 0.98 eV. The overpotential can then be

calculated as the activation free energy of the RDS divided by e or the difference between 1.23 V and the limiting potential (see eqn (15)). Therefore, the overpotential for the ORR on Pt(100), Pt(110), and Pt(111) surfaces is estimated to be 0.98, 0.96, and 0.52 V, respectively. This suggests a decreasing ORR activity trend for Pt surfaces in the order of (111) > (110) > (100). Notably, this result is in good agreement with both prior experimental findings[87] and recent results reported by Dong et al.[83] utilizing Raman spectroscopy. In the same work, the authors also performed a similar computational study. According to their presented data, the RDS on all surfaces is interpreted as the last hydrogenation step: *OH + (H$^+$ + e$^-$) → * + H$_2$O. The different RDSs between our and their data are unclear to us but probably come from the fact that (i) a significantly smaller model was employed in their models, therefore accounting for higher adsorption coverage, and (ii) different configurations were used. For instance, the higher adsorption coverage leads to unfavored chemisorption, e.g., the adsorption free energy on Pt(100) is positive.

The ORR mechanisms on Pt(100)@C, Pt(110)@C, and Pt(111)@C surfaces are depicted in Fig. 6. Similar to the Pt bare surfaces, the associated mechanism involves the same intermediates. To the best of our knowledge, only one theoretical study has examined the ORR mechanism of a graphene-coated Pt surface.[49] In their work, Choi et al.[49] found stability in a hybrid system of graphene and a monolayer of the Pt(100)-like surface, which is active for the ORR. Their identified RDS was the third hydrogenation step (*OH–*OH + (H$^+$ + e$^-$) → *OH + H$_2$O). As we employed a Pt(100) surface with several layers, we found the RDS to be the last hydrogenation, namely *OH + (H$^+$ + e$^-$) → H$_2$O. The activation free energy for this step is estimated to be 1.03 eV, which is slightly higher than the activation free energy for the RDS on bare Pt(100) (i.e., 0.98 eV). This result suggests that Pt(100)@C should exhibit ORR reactivity comparable to Pt(100). Our results also nicely corroborate the experimental observations of Abdelhafiz et al.[88] regarding the ORR activity of thin graphene–Pt hybrid catalysts.

Although having a smaller affinity towards O$_2$ compared to the Pt(100)@C surface, the ORR mechanism on the Pt(110)@C surface does not deviate much from Pt(100)@C. Most importantly, the Pt(110)@C surface also identifies the last hydrogenation reaction as the RDS, with an activation free energy of approximately 0.82 eV. Therefore, we predict that the ORR reactivity of Pt(110)@C should be slightly better than that of Pt(100)@C. In contrast, the ORR mechanism on Pt(111)@C turns out to deviate the most from that on Pt(111) as well as the other graphene-coated surfaces. First, the adsorption free energy is significantly smaller. Second, we found two competing RDSs, the second and last hydrogenation steps, with pretty similar activation energies, 0.78 eV and 0.71 eV. Based on the activation free energy of the RDS, we predict the overpotential values of Pt(100)@C, Pt(110)@C, and Pt(111)@C to be 1.03, 0.82, and 0.78 V. Thus, the ORR reactivity of graphene-coated surfaces can be ordered as Pt(111)@C > Pt(110)@C > Pt(100)@C. This order parallels the order found on the bare surfaces.

10718 | Phys. Chem. Chem. Phys., 2024, **26**, 10711–10722

This journal is © the Owner Societies 2024

Among the six surfaces studied, the bare Pt(111) surface turns out to have the smallest overpotential (*i.e.*, 0.53 V), closely followed by Pt(111)@C (*i.e.*, 0.78 V) and Pt(110)@C (*i.e.*, 0.82 V). In contrast, the Pt(100)@C surface displays significantly larger overpotential values (approximately 1.0 V). Although the results suggest that Pt(111)@C possesses slightly lower catalytic reactivity compared to the pristine Pt(111) surface, our findings highlight the dual role of graphene. On the one hand, graphene enhances the durability and stability of the catalyst by serving as a physical barrier, preventing Pt aggregation.[88-90] On the other hand, graphene-coated Pt surfaces can still catalyze the ORR with a competing catalytic reactivity compared to the pristine Pt surface. Notably, introducing defects in graphene, leading to Pt exposure to O_2, can further enhance the activity of Pt@C.[90]

3.4. ORR mechanism on the N-doped graphene-coated Pt surface

Considering the higher reactivity observed in the Pt(111)@C surface, coupled with the established effectiveness of nitrogen-doped carbon materials as metal-free catalysts for the oxygen reduction reaction (ORR),[91] we briefly discuss the ORR mechanism on a nitrogen-doped Pt(111)@C surface (also referred to as graphitic-N defects),[92] denoted as Pt(111)@C/N. Accordingly, the doping of nitrogen on the graphene coating is anticipated to exhibit better ORR activity due to (i) a higher concentration of protons, which can facilitate four-electron reduction, and (ii) enhanced O_2 adsorption capabilities.[93]

The calculated ORR mechanism on Pt(111)@C/N, in comparison with the Pt(111)@C surface, is illustrated in Fig. 7. First, we investigated different locations of nitrogen on graphene. We found that nitrogen is preferably located on the hollow site

of the top Pt layer, thus preserving its sp^2 character. Consequently, the three carbon atoms binding with this nitrogen (denoted as C^N) reside on the top sites of the Pt layer. Upon bonding with Pt, the hybridization of these carbons changes to sp^3. Here, we only explored the adsorption of O_2 in the vicinity of the nitrogen and C^N atoms, aiming at probing the impact of nitrogen. Most importantly, we found that O_2 neither adsorbs on nitrogen nor these three C^N atoms due to a lack of dangling bonds. This behavior is different from the adsorption of O_2 on nitrogen-doped carbon materials, in which the active sites are C^N.[94] On this Pt(111)@C/N surface, the most favorable adsorption configuration is observed when O_2 adopts an end-on (or Pauling) configuration on the carbon atoms bonding to C^N. Similar to the behavior observed for O_2 on Pt(111)@C, O_2 on Pt(111)@C/N can be characterized as a superoxide O_2^-, as approximately 0.8 electrons are transferred from the surface to O_2 [see Fig. 8(a)]. The slightly reduced charge transfer on Pt(111)@C/N compared to Pt(111)@C (*i.e.*, 0.98 electrons) probably comes from the end-on adsorption configuration. The adsorption energy on Pt(111)@C/N is around −0.3 eV, which is approximate to the adsorption energy on Pt(111)@C.

The major distinction between the ORR on Pt(111)@C/N and Pt(111)@C lies in the hydrogenation product of $*O_2$. As mentioned above, the ORR mechanism on Pt(111)@C is expected to proceed *via* the *O–*OH intermediate, as it is significantly more stable than the *OOH intermediate. On Pt(111)@C/N, only *OOH is formed, a feature attributed to the inability of N and C^N to provide dangling bonds to oxygen. As a result, the ORR mechanism on Pt(111)@C/N takes a distinct pathway involving *OOH, *O–H_2O, and *OH–H_2O intermediates [Fig. 7(b)]. The second hydrogenation from *OOH to *O–H_2O is similar to findings observed in an iron-embedded N-doped graphene
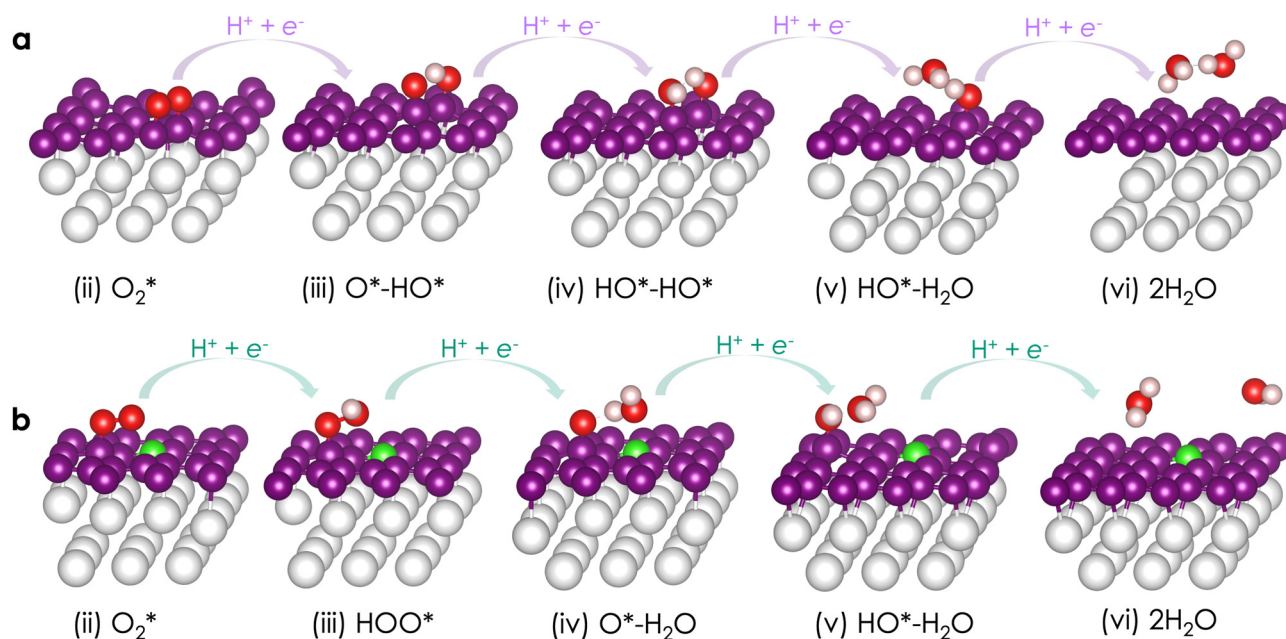

Fig. 7 Comparison of the ORR mechanism on (a) Pt(111)@C and (b) Pt(111)@C/N surfaces at five intermediates (ii–vi). The green, red, purple, grey, and white balls represent N, O, C, Pt, and H atoms, respectively.
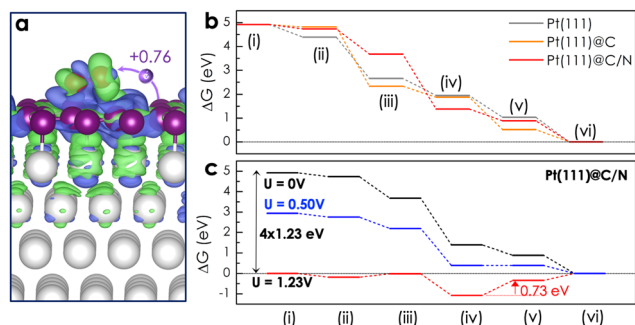
This journal is © the Owner Societies 2024

Phys. Chem. Chem. Phys., 2024, **26**, 10711–10722 | **10719**

Fig. 8 (a) Charge transfers between O_2 and the Pt(111)@C/N surface. Color code: green: gaining electron region, blue: losing electron region (isosurface value of 0.002 e bohr^{-3}). (b) Free energy profile of the ORR on the Pt(111), Pt(111)@C, and Pt(111)@C/N surfaces at U_{RHE} = 0 V. (c) Free energy profile of the ORR on the Pt(111)@C/N surface at U_{RHE} = 0 V (in black), U_{RHE} = 1.23 V (in red), and limiting potential U_L (in blue).

catalyst.[95] The third hydrogenation *O–H_2O + (H^+ + e^-) → *OH–H_2O turns out to be the RDS, with an activation free energy of 0.73 eV. Finally, the remaining *OH species undergoes hydrogenation, leading to the release of water molecules from the surface. The activation free energy of 0.73 eV is slightly smaller than that of the Pt(111)@C surface (*i.e.*, 0.78 eV), suggesting a small enhancement in ORR catalytic reactivity on the N-doped surface [Fig. 8(b and c)]. These results affirm the potential of the as prepared N-doped graphene-encapsulated PtFe alloy core–shell catalyst in our lab previously.[34,41]

4. Conclusions

In summary, we performed first-principles calculations to gain insight into the geometric and electronic properties of bare Pt surfaces, graphene- and N-doped graphene-coated Pt surfaces, as well as the mechanism of oxygen reduction reactions on these surfaces. We show that O_2 is strongly adsorbed on the bare Pt surfaces, whereas the adsorption on graphene-coated surfaces is slightly weaker. We then found that different bare Pt surfaces behaved differently in ORR catalytic activities, with the most efficient facets ordered as Pt(111) > Pt(110) > Pt(100). On the other hand, due to having a lower affinity towards O_2, the graphene-coated surfaces display different rate-determining steps. By considering only the activation energies of the rate-determining steps, the catalytic activity follows the order of Pt(111)@C > Pt(110)@C > Pt(100)@C. Estimated overpotentials indicated comparable ORR catalytic activity between the graphene-coated surfaces and bare Pt surfaces. Our calculations also highlight the dual role of the graphene coating. On the one hand, it improves the stability of the catalyst, for instance, by inhibiting the aggregation of Pt nanoparticles. On the other hand, it can actively participate in the reaction mechanism. Finally, we also pointed out that the introduction of nitrogen on the Pt(111)@C surface could potentially enhance the ORR activity by reducing the overpotential. The activity of Pt(111)@C and Pt(111)@C/N, together with the fact that they possess good stability owing to the graphene layer, have

demonstrated the potential of graphene-encapsulated Pt-based nanoparticle catalysts for the ORR.[34,41]

Conflicts of interest

There are no conflicts to declare.

Acknowledgements

Notes and references

1 D. Gielen, F. Boshell, D. Saygin, M. D. Bazilian, N. Wagner and R. Gorini, *Energy Strategy Rev.*, 2019, **24**, 38–50.
2 M. Victoria, N. Haegel, I. M. Peters, R. Sinton, A. Jäger-Waldau, C. del Canizo, C. Breyer, M. Stocks, A. Blakers, I. Kaizuka, K. Komoto and A. Smets, *Joule*, 2021, **5**, 1041–1056.
3 H. N. Nam, K. Suzuki, A. Masago, T. Q. Nguyen, H. Shinya, T. Fukushima and K. Sato, *Appl. Phys. Lett.*, 2022, **120**, 143903.
4 H. N. Nam, Q. M. Phung, K. Suzuki, H. Shinya, A. Masago, T. Fukushima and K. Sato, *J. Mater. Chem. A*, 2024, **12**, 451–459.
5 H. N. Nam, Q. M. Phung, K. Suzuki, A. Masago, H. Shinya, T. Fukushima and K. Sato, *ACS Appl. Mater. Interfaces*, 2023, **15**, 43871–43879.
6 H. N. Nam, K. Suzuki, A. Masago, H. Shinya, T. Fukushima and K. Sato, *Jpn. J. Appl. Phys.*, 2023, **62**, 020904.
7 H. N. Nam, K. Suzuki, T. Q. Nguyen, A. Masago, H. Shinya, T. Fukushima and K. Sato, *Phys. Rev. B*, 2022, **105**, 075205.
8 H. N. Nam, R. Yamada, H. Okumura, T. Q. Nguyen, K. Suzuki, H. Shinya, A. Masago, T. Fukushima and K. Sato, *Phys. Chem. Chem. Phys.*, 2021, **23**, 9773–9784.
9 M. T. Islam, M. Nabi, M. Arefin, K. Mostakim, F. Rashid, N. Hassan, S. Rahman, S. McIntosh, B. Mullins and S. Muyeen, *Heliyon*, 2022, **8**, e11836.
10 H. Yuan, Y. Hou, I. M. Abu-Reesh, J. Chen and Z. He, *Mater. Horiz.*, 2016, **3**, 382–401.
11 J. Li, W. Xia, Y. Guo, R. Qi, X. Xu, D. Jiang, T. Wang, Y. Sugahara, J. He and Y. Yamauchi, *Chem. Eng. J.*, 2023, **477**, 146841.
12 Y. Zhao, H. Nara, D. Jiang, T. Asahi, S. M. Osman, J. Kim, J. Tang and Y. Yamauchi, *Small*, 2023, **19**, 2304450.
13 M. Liu, X. Xiao, Q. Li, L. Luo, M. Ding, B. Zhang, Y. Li, J. Zou and B. Jiang, *J. Colloid Interface Sci.*, 2022, **607**, 791–815.
14 S. G. Ji, H. C. Kwon, T.-H. Kim, U. Sim and C. H. Choi, *ACS Catal.*, 2022, **12**, 7317–7325.
15 M. Che, *Catal. Today*, 2013, **218**, 162–171.
16 L. Chong, J. Wen, J. Kubal, F. G. Sen, J. Zou, J. Greeley, M. Chan, H. Barkholtz, W. Ding and D.-J. Liu, *Science*, 2018, **362**, 1276–1281.

10720 | *Phys. Chem. Chem. Phys.*, 2024, **26**, 10711–10722

This journal is © the Owner Societies 2024

17 W. Chen, J. Huang, J. Wei, D. Zhou, J. Cai, Z.-D. He and Y.-X. Chen, *Electrochem. Commun.*, 2018, **96**, 71–76.

18 W.-J. Lee, S. Bera, H.-J. Woo, W. Hong, J.-Y. Park, S.-J. Oh and S.-H. Kwon, *Chem. Eng. J.*, 2022, **442**, 136123.

19 X. Xiao, L. Zou, H. Pang and Q. Xu, *Chem. Soc. Rev.*, 2020, **49**, 301–331.

20 S. Wu, X. Qu, J. Zhu, X. Liu, H. Mao, K. Wang, G. Zhou, J. Chi and L. Wang, *J. Alloys Compd.*, 2023, 172518.

21 X. Chen, Y. Li and X. Zhao, *Surf. Interfaces*, 2023, **38**, 102821.

22 H. Zhang, S. Hwang, M. Wang, Z. Feng, S. Karakalos, L. Luo, Z. Qiao, X. Xie, C. Wang and D. Su, *et al.*, *J. Am. Chem. Soc.*, 2017, **139**, 14143–14149.

23 K. Liu, J. Fu, Y. Lin, T. Luo, G. Ni, H. Li, Z. Lin and M. Liu, *Nat. Commun.*, 2022, **13**, 2075.

24 N. Wang, S. Gan, Y. Mao, J. Xiao, C. Xu and T. Zhou, *Phys. Chem. Chem. Phys.*, 2024, **26**, 2449–2456.

25 W. Zhang, J.-K. Pan, Y.-F. Yu, X.-J. Zhang, J.-H. Wang, W.-X. Chen and G.-L. Zhuang, *Phys. Chem. Chem. Phys.*, 2023, **25**, 11673–11683.

26 Y. Li, Y. Feng, D. Zheng, X. Zhao, Y. Zhou, X. Fu and X. Chen, *J. Chem. Eng.*, 2023, **476**, 146753.

27 Z. Xue, X. Zhang, J. Qin and R. Liu, *J. Energy Chem.*, 2021, **55**, 437–443.

28 X. Lv, W. Wei, H. Wang, B. Huang and Y. Dai, *Appl. Catal., B*, 2020, **264**, 118521.

29 R. K. Ahluwalia, D. D. Papadias, N. N. Kariuki, J.-K. Peng, X. Wang, Y. Tsai, D. G. Graczyk and D. J. Myers, *J. Electrochem. Soc.*, 2018, **165**, F3024–F3035.

30 M. F. Labata, G. Li, J. Ocon and P.-Y. A. Chuang, *J. Power Sources*, 2021, **487**, 229356.

31 A. G. Manjón, M. Vega-Paredes, V. Berova, T. Gänsler, T. Schwarz, N. A. R. Rivas, K. Hengge, T. Jurzinsky and C. Scheu, *Nanoscale*, 2022, **14**, 18060–18069.

32 Q. Li, L. Wu, G. Wu, D. Su, H. Lv, S. Zhang, W. Zhu, A. Casimir, H. Zhu and A. Mendoza-Garcia, *et al.*, *Nano Lett.*, 2015, **15**, 2468–2473.

33 N. Aoki, H. Inoue, H. Kawasaki, H. Daimon, T. Doi and M. Inaba, *J. Electrochem. Soc.*, 2018, **165**, F737.

34 J.-H. Park, K. Kim, X. Wang, M. Huda, Y. Sawada, Y. Matsuo, N. Saito and M. Kawasumi, *J. Power Sources*, 2023, **580**, 233419.

35 H.-J. Choi, S.-M. Jung, J.-M. Seo, D. W. Chang, L. Dai and J.-B. Baek, *Nano Energy*, 2012, **1**, 534–551.

36 M. B. Burkholder, F. B. A. Rahman, E. H. Chandler Jr, J. Regalbuto, B. Gupton and J. M. M. Tengco, *Carbon Trends*, 2022, 100196.

37 H. Yamada, H. Kato and K. Kodama, *J. Electrochem. Soc.*, 2020, **167**, 084508.

38 S. He, Y. Liu, H. Zhan and L. Guan, *ACS Catal.*, 2021, **11**, 9355–9365.

39 M. Karuppannan, Y. Kim, S. Gok, E. Lee, J. Y. Hwang, J.-H. Jang, Y.-H. Cho, T. Lim, Y.-E. Sung and O. J. Kwon, *Energy Environ. Sci.*, 2019, **12**, 2820–2829.

40 H. Kim, A. W. Robertson, S. O. Kim, J. M. Kim and J. H. Warner, *ACS Nano*, 2015, **9**, 5947–5957.

41 P. Q. Phan, R. Naraprawatphong, P. Pornaroontham, J. Park, C. Chokradjaroen and N. Saito, *Mater. Adv.*, 2021, **2**, 322–335.

42 J. Bai, Q. Zhu, Z. Lv, H. Dong, J. Yu and L. Dong, *Int. J. Hydrogen Energy*, 2013, **38**, 1413–1418.

43 P. Rodrguez-Kessler and A. Rodrguez-Domnguez, *J. Chem. Phys.*, 2015, **143**, 184312.

44 L. Sementa, O. Andreussi, W. A. Goddard III and A. Fortunelli, *Catal. Sci. Technol.*, 2016, **6**, 6901–6909.

45 P. L. Rodrguez-Kessler, A. Muñoz-Castro, A. R. Rodrguez-Domnguez and J. L. Cabellos, *Phys. Chem. Chem. Phys.*, 2023, **25**, 4764–4772.

46 A. Panchenko, M. Koper, T. Shubina, S. Mitchell and E. Roduner, *J. Electrochem. Soc.*, 2004, **151**, A2016.

47 B. Han, V. Viswanathan and H. Pitsch, *J. Phys. Chem. C*, 2012, **116**, 6174–6183.

48 Z. Duan and G. Wang, *J. Phys. Chem. C*, 2013, **117**, 6284–6292.

49 J. I. Choi, H. S. Kim, Y.-J. Sohn, S.-D. Yim, F. M. Alamgir and S. S. Jang, *ACS Appl. Nano Mater.*, 2021, **4**, 1067–1075.

50 J. A. Keith, G. Jerkiewicz and T. Jacob, *ChemPhysChem*, 2010, **11**, 2779–2794.

51 A. Eichler and J. Hafner, *Phys. Rev. Lett.*, 1997, **79**, 4481.

52 D.-H. Lim and J. Wilcox, *J. Phys. Chem. C*, 2012, **116**, 3653–3660.

53 N. Jin, J. Han, H. Wang, X. Zhu and Q. Ge, *Int. J. Hydrogen Energy*, 2015, **40**, 5126–5134.

54 R. Zhang, N. Shehzad, L. Zhang, A. Ali, B. Amin and I. Shahid, *Chem. Phys.*, 2023, **570**, 111888.

55 J.-K. Sun, Y.-W. Pan, M.-Q. Xu, L. Sun, S. Zhang, W.-Q. Deng and D. Zhai, *Nano Res.*, 2023, 1–8.

56 P. E. Blöchl, *Phys. Rev. B: Condens. Matter Mater. Phys.*, 1994, **50**, 17953.

57 P. Giannozzi, S. Baroni, N. Bonini, M. Calandra, R. Car, C. Cavazzoni, D. Ceresoli, G. L. Chiarotti, M. Cococcioni, I. Dabo, A. D. Corso, S. de Gironcoli, S. Fabris, G. Fratesi, R. Gebauer, U. Gerstmann, C. Gougoussis, A. Kokalj, M. Lazzeri, L. Martin-Samos, N. Marzari, F. Mauri, R. Mazzarello, S. Paolini, A. Pasquarello, L. Paulatto, C. Sbraccia, S. Scandolo, G. Sclauzero, A. P. Seitsonen, A. Smogunov, P. Umari and R. M. Wentzcovitch, *J. Phys.: Condens. Matter*, 2009, **21**, 395502.

58 A. Dal Corso, *Comput. Mater. Sci.*, 2014, **95**, 337–350.

59 J. P. Perdew, K. Burke and M. Ernzerhof, *Phys. Rev. Lett.*, 1996, **77**, 3865.

60 S. Grimme, J. Antony, S. Ehrlich and H. Krieg, *J. Chem. Phys.*, 2010, **132**, 154104.

61 B. Hammer and J. K. Nørskov, *Surf. Sci.*, 1995, **343**, 211–220.

62 B. Hammer and J. K. Nørskov, *Advances in catalysis*, Elsevier, 2000, vol. 45, pp. 71–129.

63 A. H. Larsen, J. J. Mortensen, J. Blomqvist, I. E. Castelli, R. Christensen, M. Dułak, J. Friis, M. N. Groves, B. Hammer and C. Hargus, *et al.*, *J. Phys.: Condens. Matter*, 2017, **29**, 273002.

64 C. Fu, C. Liu, T. Li, X. Zhang, F. Wang, J. Yang, Y. Jiang, P. Cui and H. Li, *Comput. Mater. Sci.*, 2019, **170**, 109202.

65 J.-W. Chen, Z. Zhang, H.-M. Yan, G.-J. Xia, H. Cao and Y.-G. Wang, *Nat. Commun.*, 2022, **13**, 1734.

This journal is © the Owner Societies 2024

Phys. Chem. Chem. Phys., 2024, **26**, 10711–10722 | **10721**

66 J. K. Nørskov, J. Rossmeisl, A. Logadottir, L. Lindqvist, J. R. Kitchin, T. Bligaard and H. Jonsson, *J. Phys. Chem. B*, 2004, **108**, 17886–17892.

67 S. K. Iyemperumal and N. A. Deskins, *ChemPhysChem*, 2017, **18**, 2171–2190.

68 Q. Wang, R. Pang and X. Shi, *J. Phys. Chem. C*, 2015, **119**, 22534–22541.

69 A. J. Martnez-Galera, N. Nicoara, J. I. Martnez, Y. J. Dappe, J. Ortega and J. M. Gómez-Rodrguez, *J. Phys. Chem. C*, 2014, **118**, 12782–12788.

70 M. Cattelan, G. Peng, E. Cavaliere, L. Artiglia, A. Barinov, L. T. Roling, M. Favaro, I. Pš, S. Nappini and E. Magnano, *et al.*, *Nanoscale*, 2015, **7**, 2450–2460.

71 B. Hammer and J. K. Norskov, *Nature*, 1995, **376**, 238–240.

72 B. Hammer, Y. Morikawa and J. K. Nørskov, *Phys. Rev. Lett.*, 1996, **76**, 2141.

73 Y. Yao, Q. Fu, Y. Zhang, X. Weng, H. Li, M. Chen, L. Jin, A. Dong, R. Mu and P. Jiang, *et al.*, *Proc. Natl. Acad. Sci. U. S. A.*, 2014, **111**, 17023–17028.

74 H. Yan, B. Xu, S. Shi and C. Ouyang, *J. Appl. Phys.*, 2012, **112**, 104316.

75 H. Guang, M. Aoki, S. Tanaka and M. Kohyama, *Trans. Mater. Res. Soc. Jpn.*, 2013, **38**, 477–480.

76 F. R. Bagsican, A. Winchester, S. Ghosh, X. Zhang, L. Ma, M. Wang, H. Murakami, S. Talapatra, R. Vajtai and P. M. Ajayan, *et al.*, *Sci. Rep.*, 2017, **7**, 1774.

77 H. Shin, Y. Luo, A. Benali and Y. Kwon, *Phys. Rev. B*, 2019, **100**, 075430.

78 Z. Shi, J. Zhang, Z.-S. Liu, H. Wang and D. P. Wilkinson, *Electrochim. Acta*, 2006, **51**, 1905–1916.

79 A. Lahee, W. Allison, R. Willis and K. Rieder, *Surf. Sci.*, 1983, **126**, 654–660.

80 G. Kellogg, *Phys. Rev. Lett.*, 1985, **55**, 2168.

81 E. C. Sowa, M. Van Hove and D. Adams, *Surf. Sci.*, 1988, **199**, 174–182.

82 A. Walker, B. Klötzer and D. King, *J. Chem. Phys.*, 1998, **109**, 6879–6888.

83 J.-C. Dong, X.-G. Zhang, V. Briega-Martos, X. Jin, J. Yang, S. Chen, Z.-L. Yang, D.-Y. Wu, J. M. Feliu and C. T. Williams, *et al.*, *Nat. Energy*, 2019, **4**, 60–67.

84 V. Gueskine, A. Singh, M. Vagin, X. Crispin and I. Zozoulenko, *J. Phys. Chem. C*, 2020, **124**, 13263–13272.

85 Z. Duan and G. Wang, *Phys. Chem. Chem. Phys.*, 2011, **13**, 20178–20187.

86 G.-L. Chai, Z. Hou, D.-J. Shu, T. Ikeda and K. Terakura, *J. Am. Chem. Soc.*, 2014, **136**, 13629–13640.

87 A. M. Gómez-Marn, R. Rizo and J. M. Feliu, *Catal. Sci. Technol.*, 2014, **4**, 1685–1698.

88 A. Abdelhafiz, A. Vitale, P. Buntin, B. deGlee, C. Joiner, A. Robertson, E. M. Vogel, J. Warner and F. M. Alamgir, *Energy Environ. Sci.*, 2018, **11**, 1610–1616.

89 C. D. Jaimes-Paez, E. Morallón and D. Cazorla-Amorós, *Energy*, 2023, **278**, 127888.

90 D. Liu, J. Zhang, D. Liu, T. Li, Y. Yan, X. Wei, Y. Yang, S. Yan and Z. Zou, *J. Phys. Chem. Lett.*, 2022, **13**, 2019–2026.

91 Q. Lv, W. Si, J. He, L. Sun, C. Zhang, N. Wang, Z. Yang, X. Li, X. Wang and W. Deng, *et al.*, *Nat. Commun.*, 2018, **9**, 3376.

92 A. Martn-Recio, C. Romero-Muñiz, P. Pou, R. Pérez and J. M. Gómez-Rodrguez, *Nanoscale*, 2016, **8**, 17686–17693.

93 D. Deng, L. Yu, X. Chen, G. Wang, L. Jin, X. Pan, J. Deng, G. Sun and X. Bao, *Angew. Chem., Int. Ed.*, 2013, **52**, 371–375.

94 D. Guo, R. Shibuya, C. Akiba, S. Saji, T. Kondo and J. Nakamura, *Science*, 2016, **351**, 361–365.

95 A. F. Z. Abidin and I. Hamada, *Surf. Sci.*, 2022, **724**, 122144.

10722 | *Phys. Chem. Chem. Phys.*, 2024, **26**, 10711–10722

This journal is © the Owner Societies 2024